Materials Science

AIMS Materials Science, 10(2): 342–355.
DOI: 10.3934/matersci.2023018
Received: 19 October 2022
Revised: 13 March 2023
Accepted: 22 March 2023
Published: 31 March 2023

http://www.aimspress.com/journal/Materials

Research article

Demonstration of ferroelectricity in PLD grown HfO_2-ZrO_2 nanolaminates

Sree Sourav Das[1,*], Zach Fox[1], Md Dalim Mia[2], Brian C Samuels[2], Rony Saha[2], and Ravi Droopad[1,2]

[1] Ingram School of Engineering, Texas State University, San Marcos, TX-78666, USA
[2] Materials Science, Engineering and Commercialization, Texas State University, San Marcos, TX-78666, USA

* **Correspondence:** Email: xky3tv@virginia.edu; Tel: +1-737-213-3051.

Abstract: Ferroelectricity is demonstrated for the first time in Si(100)/SiO_2/TiN/HfO_2-ZrO_2/TiN stack using pulsed laser deposition (PLD) and the effects of temperatures, partial oxygen pressures, and thickness for the stabilization of the ferroelectric phase were mapped. Thin films deposited at a higher temperature and a higher oxygen partial pressure have a higher thickness, demonstrating a better ferroelectric response with ~12 $\mu C/cm^2$ remnant polarization, a leakage current of 10^{-7} A (at 8 V) and endurance >10^{11} cycles indicative of an orthorhombic crystal phase. In contrast, thin films deposited at lower temperatures and pressures does not exhibit ferroelectric behavior. These films can be attributed to having a dominant monoclinic phase, having lower grain size and increased leakage current. Finally, the effects of ZrO_2 as top and bottom layer were also investigated which showed that ZrO_2 as the top layer provided better mechanical confinement for stabilizing the orthorhombic phase instead of as the bottom layer.

Keywords: ferroelectricity; pulsed laser deposition; remnant polarization; leakage current; endurance; X-ray diffraction

1. Introduction

In the advancement of emerging technologies such as IoT, big data, cloud computing, etc., traditional memory technologies face challenges due to high power loss, limited endurance, low

write speed, and scalability issues [1,2]. To overcome the aforementioned drawbacks and meet the increasing demands for information technology, novel and high-performance memory is urgently needed. Recently, ferroelectric materials having bi-stable polarization states in electric field-induced hysteresis response have garnered enormous interest for next-generation memory applications, known as FeRAM (Ferroelectric Random Access Memory) [3,4]. Initially, perovskite and related structures such as $BaTiO_3$, $PbTiO_3$, $SrBi_2Ta_2O_9$, Bi_4Ti_3O, PZT, etc. [5–11] possessed a significant amount of attraction for FeRAMs due to their large remnant polarization, chemical and thermal stability. However, despite having excellent characteristics, perovskite materials suffer from lower dielectric constant, and face severe scaling limitations due to having a small bandgap of 3.2–4.3 eV [12]. Thus, thicker films of perovskite materials are required to avoid leakage current which is undesirable for the implementation in high-density memory technologies [3]. It is also challenging to integrate these materials in memory devices because of their complicated structure. However, the recent discovery of ferroelectricity in HfO_2-based materials and $HfZrO_4$ have resolved the aforementioned critical issues of perovskite-structure ferroelectrics [13]. Ferroelectricity in HfO_2 is promising due to its compatibility with Si CMOS technology since it is currently being used as a high-k dielectric material. In addition, HfO_2-based materials demonstrate high remnant polarization with downsizing to 5 nm due to its high electronic bandgap of 5–5.9 eV [14] compared to perovskite materials [15,16]. Furthermore, HfO_2-based ferroelectrics can withstand annealing in forming gas (N_2 + 4% H_2) without degradation of polarization compared to conventional perovskite-based ferroelectrics, making this material system more compatible with modern semiconductor integration schemes. Hence, HfO_2-based ferroelectric memories are promising candidates due to its scalability, chemical structure, improved polarization switching and endurance performance.

Primarily, HfO_2 is stable in a monoclinic phase at room temperature (RT) and transforms into a higher symmetry tetragonal phase at 1720 °C. With further increase in temperature, the tetragonal phase (t-phase) transforms into a cubic phase (c-phase) at 2700 °C [4]. These centrosymmetric phases, however, are not responsible for the ferroelectricity in HfO_2. Ferroelectricity in HfO_2 originates from the non-centrosymmetric orthorhombic phase (o-phase) with space group Pca_{21} which was first proposed in Mg-doped ZrO_2 using neutron diffraction and also confirmed by Sang et al. using scanning transmission electron microscopy (STEM) [4,17,18]. Various driving factors such as doping, surface effects, film thickness, annealing temperature [19], oxygen vacancies, capping electrode [4,20], etc. need to be considered in stabilizing this metastable o-phase at room temperature.

Ferroelectricity in HfO_2 has been investigated by chemical doping using Y [18], Zr [21], Si [22], La [23], Gd [24] and other metallic elements [13]. The most intensively studied system is the HfO_2-ZrO_2 alloy/solid solution, as these binaries have a similar ionic size and chemical valence and exhibit lower crystallization temperatures compared to pure HfO_2 and ZrO_2 [25]. Considering these reasons, it is believed that $Hf_xZr_{1-x}O_2$ can be an extremely promising candidate in non-volatile ferroelectric memories. Recent studies show ferroelectricity over a wide composition range in $Hf_xZr_{1-x}O_2$ having maximum remnant polarization (17 $\mu C/cm^2$) [2,21,25] and endurance (10^9 cycles) for x = 0.5 on STO(100) templates grown on Si [26]. Chernikova et al. reported improved endurance up to 4×10^{10} cycles by introducing 1 mol% La in HZO film, but this endurance is not sufficient for memory applications [23]. Besides, introducing an STO template or La-doping brings complexity to the fabrication process [27]. Therefore, an alternative design has recently been proposed [3,27,28], involving bilayers or superlattices of undoped HfO_2 and ZrO_2 thin films. A bilayer system is much

simpler to design and provides better flexibility in the fabrication process over either doped-HfO_2 or a solid solution of HZO thin films, which require precise composition control. Although a single layer of HfO_2 can show ferroelectricity with a small amount of remnant polarization [29], introducing ZrO_2 as the top layer can improve the ferroelectric response by applying mechanical stress [27]. However, the study of bilayer structures is still in its early stage and an extension of the bilayer structure is the use of nanolaminates that can be deposited by a number of techniques. To the best of our knowledge, all HfO_2-ZrO_2 nanolaminate systems have been grown by Atomic Layer Deposition (ALD) at temperatures <300 °C followed by post-growth annealing at higher temperatures for crystallization [4]. The low-temperature deposition process with precursors suffers not only from the difficulty of process time but also from carbonaceous impurities in the deposited materials which degrade the quality of the film [30]. Additionally, the behavior of this nanolaminate system grown at high temperatures and different partial oxygen pressures still requires extensive study. Another suitable growth technique that offers more degrees of freedom over ALD to engineer the deposition conditions, can be carried out further to validate the behavior of ferroelectricity in HfO_2-ZrO_2 nanolaminates. In this regard, pulsed laser deposition (PLD) provides such flexibility to adjust the driving factors (temperature, oxygen pressure, and thickness) over a wide range and make the process chemical-free and non-toxic [30,31]. PLD uses ceramic targets as the source and a high-energy laser is used to transfer the source composition onto a substrate [32].

In this study, ferroelectricity is demonstrated for the first time in PLD grown HfO_2-ZrO_2 bilayer system on TiN/SiO_2/Si by optimizing the growth conditions (substrate temperatures, partial oxygen pressures, thickness, and switching layers sequence). Due to the limitations of the equipment, the maximum deposition temperature used in this study was limited to 750 °C and additionally, as we achieved fully oxidized film at an oxygen partial pressure of 1.2×10^{-4} torr, higher oxygen pressure was not considered. X-ray diffraction, polarization vs voltage (P-V) hysteresis, and Raman spectroscopy were performed on the thin films to explore the properties and origin of ferroelectricity. The result of this study will give insight and suggest possible routes to optimize this material system for memory applications.

2. Materials and methods

A 100 mm diameter p-type Si (100) wafer was first oxidized using a thermal oxidation process at a temperature of 1000 °C, with N_2 flow 5 SLM and O_2 flow 2 SLM, for 2 h 30 min. Following this, 85 nm TiN was deposited on the SiO_2/Si by DC magnetron sputtering at room temperature with an argon flow rate of 10 sccm. Later, a bilayer of the HfO_2-ZrO_2 stack was grown on the Si/SiO_2/TiN template, the structure of which is shown in Figure 1. Two separate targets of HfO_2 and ZrO_2 were used for the deposition of the HfO_2-ZrO_2 nanolaminates. Film growth was carried out using PLD, which uses a Krypton Fluoride (KrF) excimer source having a wavelength of 248 nm to ablate the target materials onto the substrate. During deposition, the laser pulse frequency was 3 Hz with an energy of 400 mJ. Three series of samples were prepared under varying deposition conditions: thickness (t), temperature (T_s) and partial oxygen pressure (P_o) series. In the thickness series, the individual layer thickness of HfO_2-ZrO_2 layers was varied by controlling the number of laser pulses at a fixed temperature of 750 °C and oxygen partial pressure of 1.2×10^{-4} torr. In the temperature series samples, a 15 nm HfO_2/15 nm ZrO_2 bilayer structure was deposited at RT, 500 °C and 750 °C at a fixed P_o of 1.2×10^{-4} torr. In the pressure series samples, the 15 nm HfO_2/15 nm ZrO_2 structure

was deposited at P_o of 1.2×10^{-4} torr and 10^{-6} torr at a constant substrate temperature of 750 °C. After deposition, the samples were cooled to RT under an oxygen partial pressure of 10^{-6} torr. A shadow mask was then used to deposit 50 nm TiN top electrode using DC magnetron sputtering followed by a 1 min annealing at 750 °C in a N_2 atmosphere for better confinement in the structure. For convenience, #H and #Z are used, where # denotes the thickness in nm, and H and Z represent HfO_2 and ZrO_2 respectively.

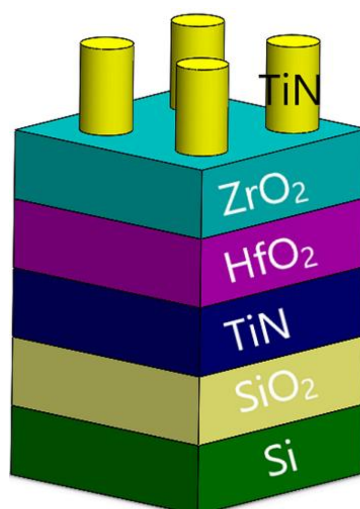

Figure 1. Typical bilayer film structure used in this study.

The crystal structure of the films was measured using a Rigaku SmartLab X-ray diffraction system with an operating voltage of 40 kV and current of 44 mA for Cu-Kα source having a wavelength of 0.1540562 nm. Symmetric XRD scans were performed on all samples to determine the phases in the films. Ferroelectric properties were measured in a top-bottom configuration (grounding the bottom electrode and biasing applied to the top) at room temperature using a Precision LC tester from Radiant Technologies.

3. Results and discussion

Figure 2 shows the XRD spectra for a series of samples having various thicknesses that were grown at a fixed temperature of 750 °C and oxygen partial pressure of 1.2×10^{-4} torr. As a reference, the XRD 2θ scans of HfO_2 and ZrO_2 are also included. Diffraction peaks around 23°, 27.5°, 48.8°, and 54° correspond to TiO_2 and 28.2°, 31.5°, 34.5°, 35.3°, 36°, and 41° can be assigned to m(-111), m(111), m(200), o(002), TiN(111), and TiN(100), respectively. Here, m, o and t represent the monoclinic, orthorhombic, and tetragonal phases, respectively. The presence of TiO_2 is due to the oxidation of Ti during the growth of HfO_2-ZrO_2 nanolaminates. The deposited thin films were polycrystalline that included a peak o(002) at around 35.3°. This peak representing the orthorhombic phase is similar to that reported in the literature [33]. Normalized high-resolution XRD (HRXRD) spectra of the samples are shown in Supplementary Information Figure S1. Further characterizations using Raman spectroscopy and electrical characterization were done to validate the presence of an orthorhombic phase over the monoclinic and tetragonal phases at this diffraction angle.

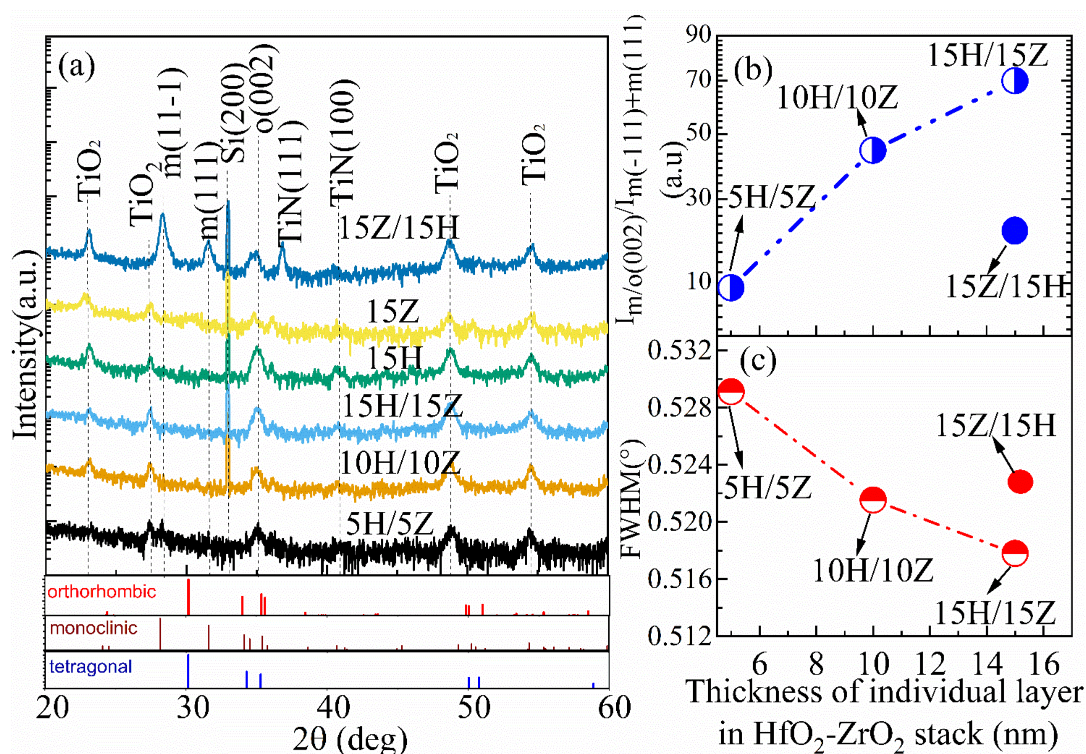

Figure 2. (a) XRD 2θ scan of HfO_2-ZrO_2 deposited at 750 ℃ and $P_o = 1.2 \times 10^{-4}$ torr for various layer thicknesses, (b) Normalized intensity of o(002) peak w.r.t m(-111), and (c) FWHM of o(002) with varying thickness: 5 nm HfO_2/5 nm ZrO_2, 10 nm HfO_2/10 nm ZrO_2, 15 nm HfO_2/15 nm ZrO_2, 15 nm ZrO_2/15 nm HfO_2, respectively. Reference powder patterns for HfO_2 and ZrO_2.

The relative intensity of the o(002) increases and full-width half maximum (FWHM) of the o(002) peak decreases with layer thickness, which implies improved crystallinity and a dominating orthorhombic phase. The relation of intensity and FWHM with layer thickness is shown in Figure 2b,c, respectively. The reason for improved crystallinity can be attributed to the large mechanical and thermal stress applied by the increased ZrO_2 layer during crystallization and subsequent cooling which brings rigidity, better confinement and stabilizes underlying HfO_2 layer. However, a single layer of 15 nm ZrO_2 also shows a small peak of o(002) [21,28].

To explore the role played by the ZrO_2-layer, a 15 nm ZrO_2 was deposited as a starting layer followed by a 15 nm HfO_2 at a fixed temperature of 750 °C and oxygen pressure of 1.2×10^{-4} torr. The properties of this structure were then compared to a similar grown structure but with the HfO_2 layer grown first followed by the ZrO_2 layer. From the 2θ scan, in Figure 2, the sample having ZrO_2 as the first layer (top spectrum) has two dominant monoclinic phases of m(11-1), m(111) at 28.22° and 31.52°, respectively, and an associated broad peak of o(002) around 35.3°. When compared with the sample having the HfO_2 layer first grown, the monoclinic phases become dominant over the orthorhombic phase in ZrO_2 starting sample. When ZrO_2 is used as starting layer, it is predicted that ZrO_2 crystallizes faster than the HfO_2 top layer and creates tensile stress on top layer resulting in reduced activation energy to transform t-phase to m-phase. This is the result of a reduced critical radius of m-phase which increases the nucleation rate of the monoclinic phase in the film [28]. The

normalized intensity ratio of o(002)/m(-111) + m(111) and FWHM also confirm the higher crystallinity of the o(002)-phase in the HfO_2-starting structure as shown in Figure 2b,c.

Figure 3 summarizes the effect of oxygen pressure on a 15 nm HfO_2/15 nm ZrO_2 bilayer structure. It is observed that the structure grown at low P_o (~10^{-6} torr) shows a predominantly monoclinic phase in addition to a small o(002) phase, while the sample grown at high P_o (~1.2×10^{-4} torr) demonstrates a dominant o(002) peak around 35.3 °. This phenomenon can be explained by considering the oxygen deficiency in the top layer of ZrO_2. This oxygen-deficient layer does not provide enough mechanical confinement to the underlying HfO_2 layer in comparison to the sample grown at high P_o. Besides, the small o(002) peak slightly shifts to a smaller diffraction angle in the reduced P_o condition indicating an increased interplanar spacing of o(002) phase favoring the formation of the monoclinic phase (m(200)). Similar behavior was also observed when an alloy of HfO_2-ZrO_2 ($Hf_{0.5}Zr_{0.5}O_2$) was grown using PLD under low oxygen conditions [34].

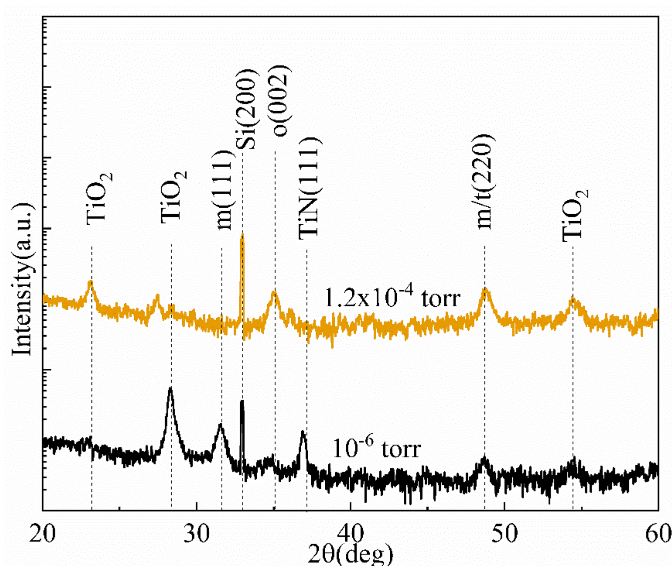

Figure 3. XRD 2θ scans of 15 nm HfO_2/15 nm ZrO_2 after deposited at 750 °C using oxygen pressures of 1.2×10^{-4} torr and 10^{-6} torr.

To study the effect of deposition temperature on the layer properties, a 15 nm HfO_2/15 nm ZrO_2 thin film structure was grown at different temperatures with a fixed oxygen partial pressure of 1.2×10^{-4} torr. The XRD spectra for the structure grown at three different temperatures are shown in Figure 4a immediately after deposition and after rapid thermal annealing (RTA) at 750 °C in Figure 4b. At room temperature deposition, the structure as grown is mostly amorphous while the structure grown at 500 °C, shows a broad peak around 35.3 °, which can be attributed to a mixture of the orthorhombic with a small amount of monoclinic phase. The structure grown at 750 °C shows a predominantly o(002) peak. After rapid thermal annealing at 750 °C for 1 min in an N_2 atmosphere, the structure grown at RT remains amorphous. Interestingly, the structure grown at 500 °C shows clear a doublet peak at 34.2 °and 35.3 °which can be assigned to the m(200) and o(002). No obvious change in the structure was observed for samples grown at 750 °C after annealing. Normalized HRXRD scan for pressure dependent and temperature dependent samples are also depicted in Supplementary Information Figures S2 and S3.

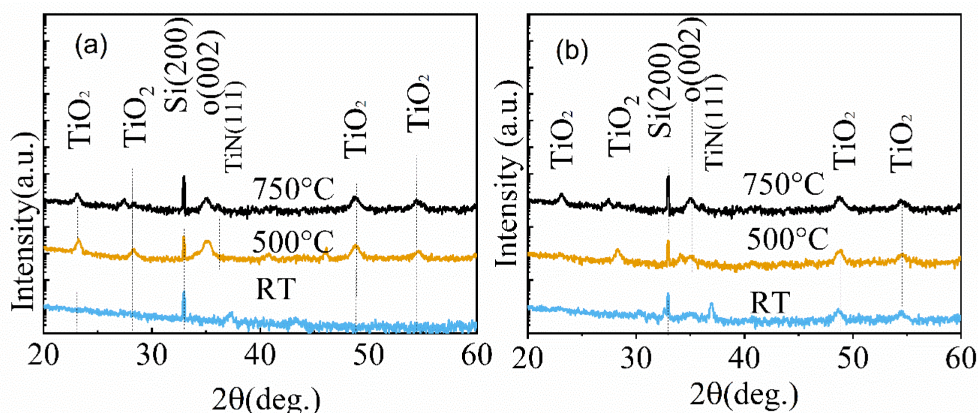

Figure 4. XRD 2θ scans of 15 nm HfO_2/15 nm ZrO_2 deposited at Po = 1.24×10^{-4} torr at different temperatures (a) after deposition and (b) after annealing at 750 °C in N_2 atmosphere for 1 min.

Previous studies suggest that different HfO_2 crystal phases show different vibrational modes in Raman spectra [35–37]. Thus, the presence of crystal phases of HfO_2 and stress on the HfO_2 layer can also be evaluated by means of Raman spectroscopic analysis. Figure 5 shows the orthorhombic peak of HfO_2 around 140 cm^{-1}, 435 cm^{-1} and 600 cm^{-1} in the Raman spectra for both single HfO_2 layer and bilayer HfO_2-ZrO_2 structures. However, a closer examination of the peak around 140 cm^{-1} (inset Figure 5) shows that the Raman peak of the bilayer structure shifts to a lower wavenumber and appears to be more intense and narrower when compared to the single-layer HfO_2 sample. This shift can be attributed to the stress caused by the ZrO_2 layer and is clearly visible from the peak shift in spectra (inset Figure 5). The peak (~142 cm^{-1}) is shifted to left by 0.41 cm^{-1} for 15 nm HfO_2-15 nm ZrO_2 compared to the 15 nm thick HfO_2 layer which is the result of in-plane tensile stress on the HfO_2 layer exerted by the top ZrO_2 layer [35]. Thus, the Raman analysis further confirms that the observed XRD peak around 35.3° can be assigned to the o(002) plane resulting from the in-plane tensile stress.

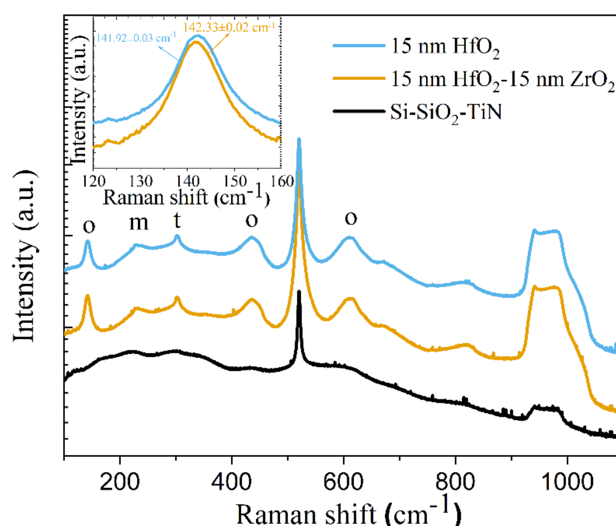

Figure 5. Raman spectroscopy for HfO_2-ZrO_2 bilayer structures.

To further confirm the presence of an orthorhombic phase, polarization-voltage (P-V) measurements were performed using a bipolar triangular pulse having an amplitude of 8 V and a frequency of 1 kHz applied by a precision LC ferroelectric tester. Leakage current was tested in DC sweep mode of −8 V to 8 V. Endurance test was carried out by bipolar rectangular pulse train having an amplitude of 8 V and pulse width of 0.05 ms. To analyze wake-up effects, P-V measurement was taken after 10^5 cycles of rectangular pulses.

Figures 6a,b show the ferroelectric polarization before and after 10^5 wake-up cycling of the thickness-dependent samples. Included in the figure are the data for bilayer structures with various individual thicknesses and data for a single layer of HfO_2 and ZrO_2. All the bilayer films showed hysteresis response in the P-V measurements which further concludes the presence of o(002) phase over the monoclinic and tetragonal phases at 35.3°. With the increase of thickness in the bilayer structure, there is an improvement of the ferroelectric polarization. Maximum remnant polarizations of 12, 9.45, 7.46, 5.9 μC/cm^2 were obtained before cycling and 11.6, 9.3, 7.4, 5 μC/cm^2 after 10^5 cycling for sample 15H/15Z, 10H/10Z, 5H/5Z, 15H, respectively. Thus, improved hysteresis response with higher remnant polarization was obtained compared to previously published data [31]. Besides, the behavior of increasing remnant polarization with thickness is consistent with a recent work on PLD-grown $Hf_{0.5}Zr_{0.5}O_2$ alloy [30] directly on Si used as a ferroelectric gate dielectric. Improved polarization with layer thickness can be explained due to an improvement in the crystallinity and enhanced orthorhombic phase in the thin film [27]. In the case of the single layer 15H, the hysteresis loop did not saturate fully even after cycling, which could be due to the absence of mechanical stress provided by the ZrO_2 layer. Another reason behind the unsaturated P-V response can be attributed to charge tunneling and lossy dielectric effect in the film [30]. In addition, no electrical polarization was observed for 15Z due to the absence of an orthorhombic phase which was confirmed by the XRD measurements. In Figure 6c, the samples did not show a significant change in polarization up to 10^{11} cycles during endurance testing indicating minimal effects relating to the reduced oxygen vacancies or defects in the structure. In comparison, endurance testing on ALD-grown samples show awake effect up to 10^4–10^5 cycle which was explained to be due to the presence of defects or oxygen vacancies [29,38]. Figure 6d shows the leakage current of the various bilayer structures. With increasing thickness, there is a decrease in the leakage current which corresponds to an increase in the grain sizes as a result of the high temperature experienced during a longer growth time.

P-V and leakage current measurements were also performed on the altered sequence structure (15Z/15H), in which the starting layer was ZrO_2, are shown in Figure 7 and were compared with the HfO_2 starting sample (15H/15Z). Remnant polarization of the ZrO_2-starting sample is significantly smaller as compared with the HfO_2-starting sample as the m-phase is more dominant in the ZrO_2-starting sample. Additionally, 15Z/15H sample shows higher leakage current due to smaller grain size in the film.

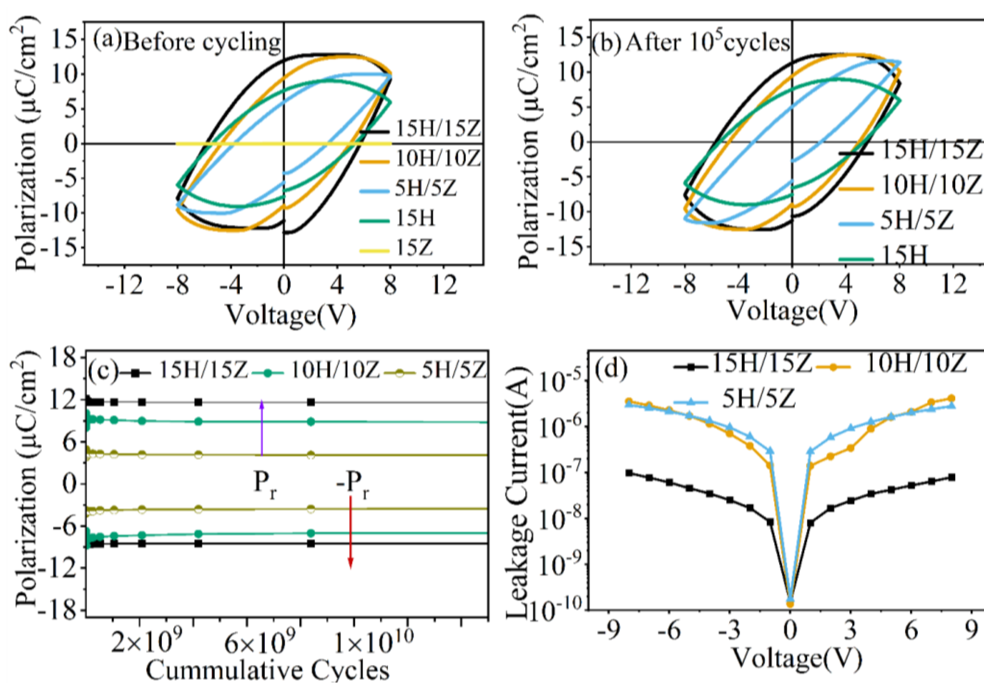

Figure 6. Ferroelectric measurement for both single layer and bilayer HfO_2-ZrO_2 structures with varying thickness: (a) P-V hysteresis loop before field cycling, (b) P-V hysteresis loop after 10^5 field cycling, (c) Endurance test and (d) Leakage current test.

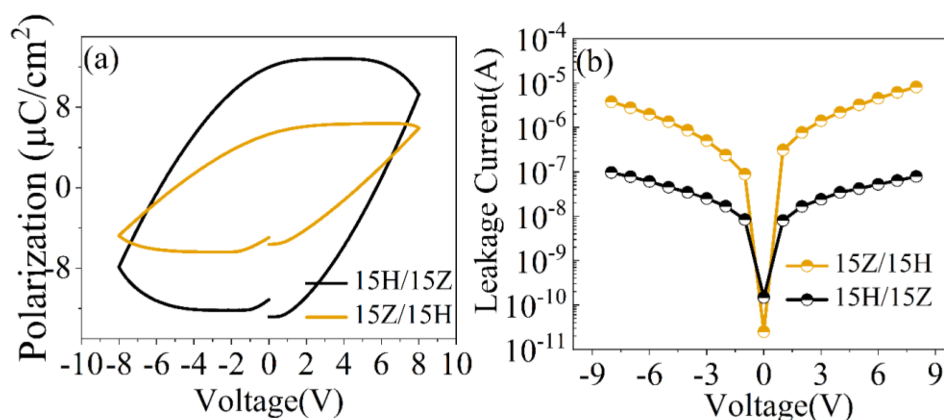

Figure 7. Ferroelectric measurement: (a) P-V hysteresis loop, (b) Leakage test for ZrO_2 starting sample and HfO_2 starting sample.

Furthermore, ferroelectric measurements of the P_o series and T_s series were taken and shown in Figure 8a,b and 8c,d. Thin films deposited at low oxygen pressure (10^{-6} torr) show a linear dielectric behavior which is consistent with the XRD data that show a dominant monoclinic phase in the film. In the T_s series, the sample grown at room temperature showed an oval shape response as expected for an ideal resistor because of high leakage current as shown in Figure 8c,d. The sample grown at 500 °C does not show remnant polarization in the P-V loop because of a higher fraction of monoclinic phase over the o-phase but at 750 °C, film showed a hysteresis loop with an improved remnant polarization due to the presence of an orthorhombic phase in the film. Even though the P-V

loops showed a lossy ferroelectric response due to our measurement setup [39], they showed good remnant polarization. The lossy part can be compensated using the Sawyer-Tower method [39]. Unfortunately, we could not carry out the Sawyer-Tower method due to the limitation of sample geometry, as shown in Figure 1.

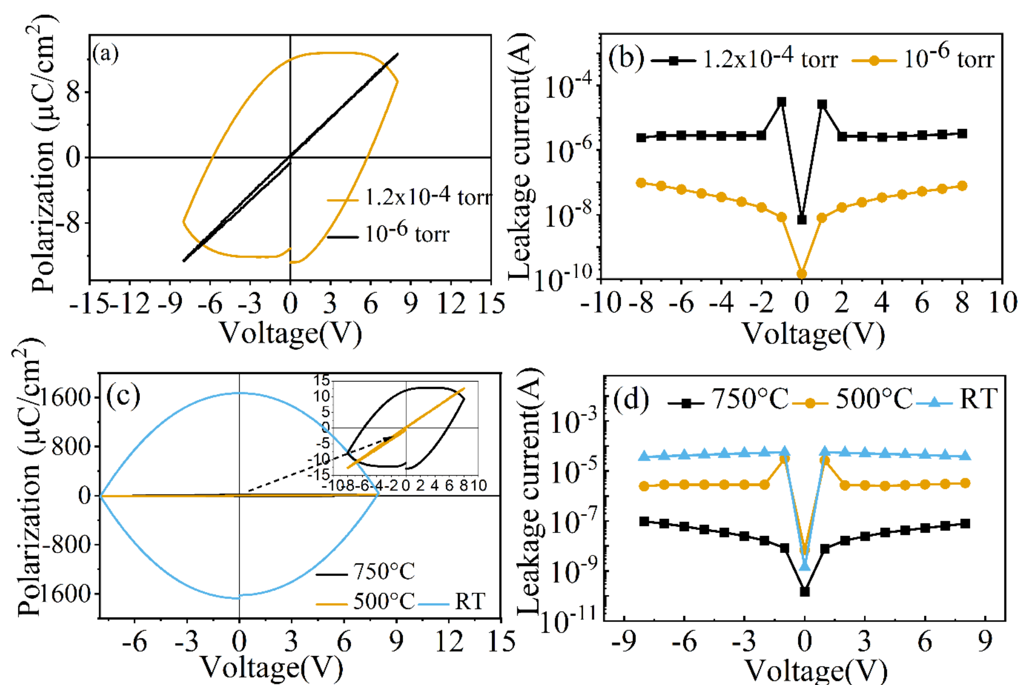

Figure 8. Ferroelectric measurement: P_o series sample (a) P-V hysteresis loop, (b) Leakage current for 15 nm HfO_2/15 nm ZrO_2 deposited at 750 °C with different oxygen pressure. T_s series sample, (c) P-V hysteresis loop of 15 nm HfO_2/15 nm ZrO_2 at room temperature (inset: at 500 °C and 750 °C), (d) Leakage current for 15 nm HfO_2/15 nm ZrO_2 at different temperatures.

Figure 9a summarizes the ferroelectric properties based on thickness, temperature, oxygen pressure and crystalline phases for the samples used in this study which were limited in growth temperature and oxygen partial pressure up to 750 °C and 1.2×10^{-4} torr, respectively. Here, t denotes the thickness series samples, T_s denotes the temperature series samples and P_o denotes the oxygen pressure series samples. The intensity of the o(002) phase and remnant polarization increases with increasing thickness, pressure, and temperature as a result of increasing mechanical stress exerted by ZrO_2 top layer in the structure. A comparative study of this work with the reported literature is illustrated in Figure 9b,c, which includes polarization and endurance of HfO_2-based ferroelectric devices with various dopants. The HfO_2-ZrO_2 nanolaminates structure of this work showed endurance $>10^{11}$ cycles, and remnant polarization of ~12 μC/cm² for the 15H/15Z, which is much higher than reported in the literature for Hf-based structures as shown in Figure 9b. Figure 9c shows the endurance versus polarization for different dopants in HfO_2 and a comparison between nanolaminates grown by PLD and ALD. Recently reported ALD deposited 4.4 nm HfO_2/4.4 nm ZrO_2 nanolaminates showed the highest remnant polarization of 17 μC/cm² [28] and endurance 4×10^{10} cycles [40] while this work found ~12 μC/cm² and endurance $>10^{11}$ cycles (which is denoted by the

red arrow in the figure) in 15H/15Z sample. The improved endurance in PLD grown samples can be attributed to reduced defects during growth.

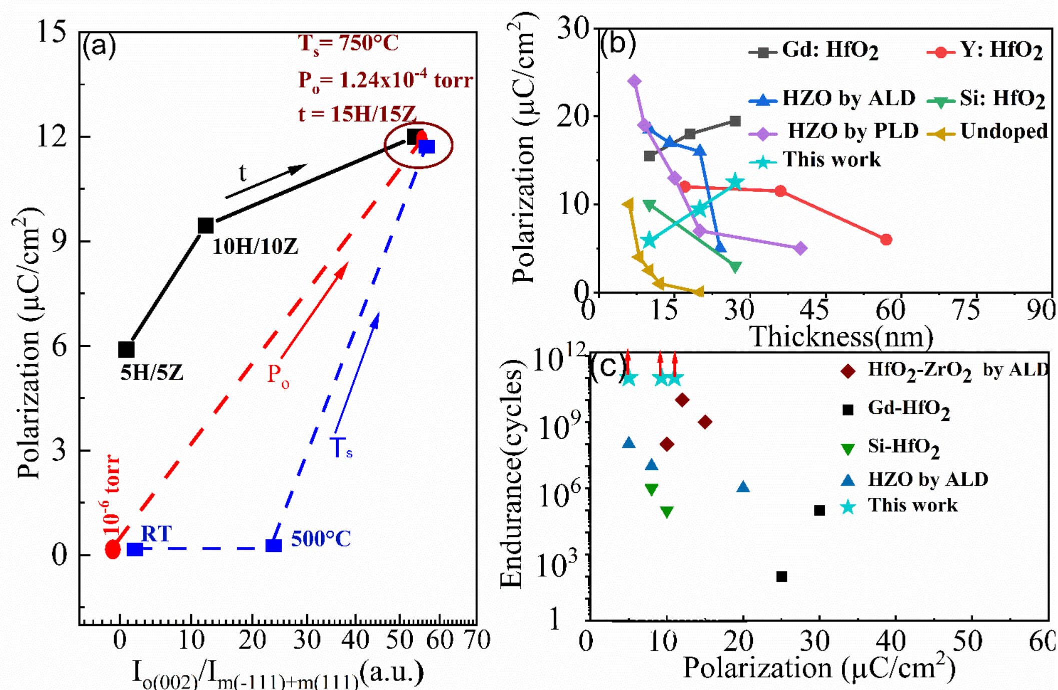

Figure 9. (a) Summary of the effects of different growth conditions (thickness, temperature, and pressure) in terms of remnant polarization and intensity of o(002) w.r.t m-phases. Here, t denotes the thickness series samples, T_s denotes temperature series samples and P_o denotes the oxygen pressure series samples. (b) A comparative study of remnant polarization depending upon thickness for different dopants (Undoped HfO_2 [29], HZO by ALD [3], HZO by PLD [26], Si: HfO_2 [22], Y: HfO_2 [18], Gd: HfO_2 [24], HfO_2-ZrO_2 by ALD [28]), (c) Endurance vs P_r diagram for various reported result compared with this study.

4. Conclusions

In conclusion, the orthorhombic phase appears to be dominant with increasing thickness in ZrO_2/HfO_2 bilayer structures and demonstrate better ferroelectric behavior when grown at elevated temperature using PLD. High temperature and partial oxygen pressure during PLD growth contribute to the improved ferroelectric polarization compared to the sample grown at low temperatures and oxygen pressures. Moreover, it was observed that ZrO_2 as a top layer demonstrates better ferroelectric performance due to the mechanical stress induced on the HfO_2 layer compared to the case when ZrO_2 is used as a bottom layer. This bilayer structure deposited by PLD showed endurance of more than 10^{11} cycles with ~12 μC/cm^2 remnant polarization which is much higher than the best result reported so far for HfO_2/ZrO_2 nanolaminates and solid solution films. This study shows that the nanolaminates structure of HfO_2-ZrO_2 deposited by PLD can be highly promising for solid-state memory applications.

Acknowledgments

This work is partly funded through a donation from the Intel Corp.

Conflict of interest

The authors declare that they have no known competing financial interests or personal relationships that could have appeared to influence the work reported in this paper.

References

1. Zhang Z, Wang Z, Shi T, et al. (2020) Memory materials and devices: From concept to application. *InfoMat* 2: 261–90. https://doi.org/10.1002/inf2.12077.
2. Bouaziz J, Rojo Romeo P, Baboux N, et al. (2019) Characterization of ferroelectric hafnium/zirconium oxide solid solutions deposited by reactive magnetron sputtering. *J Vac Sci Technol B* 37: 021203. https://doi.org/10.1116/1.5060643.
3. Weeks SL, Pal A, Narasimhan VK, et al. (2017) Engineering of ferroelectric HfO_2-ZrO_2 nanolaminates. *ACS Appl Mater Interfaces* 9: 13440–13447. https://doi.org/10.1021/acsami.7b00776.
4. Fan Z, Chen J, Wang J (2016) Ferroelectric HfO_2-based materials for next-generation ferroelectric memories. *J Adv Dielectr* 6: 1630003. https://doi.org/10.1142/S2010135X16300036
5. Lu J, Luo W, Feng J, et al. (2018) Unusual ferroelectricity in two-dimensional perovskite oxide thin films. *Nano Lett* 18: 595–601. https://doi.org/10.1021/acs.nanolett.7b04797
6. Sai N, Kolpak AM, Rappe AM (2005) Ferroelectricity in ultrathin perovskite films. *Phys Rev B* 72: 20101. https://doi.org/10.1103/PhysRevB.72.020101
7. Cohen RE (1992) Origin of ferroelectricity in perovskite oxides. *Nature* 358: 136–138. https://doi.org/10.1038/358136a0
8. Kim K, Lee S (2006) Integration of lead zirconium titanate thin films for high density ferroelectric random access memory. *J Appl Phys* 100: 51604. https://doi.org/10.1063/1.2337361
9. Martin LW, Rappe AM (2016) Thin-film ferroelectric materials and their applications. *Nat Rev Mater* 2: 1–14. https://doi.org/10.1038/natrevmats.2016.87
10. De Araujo C-P, Cuchiaro JD, McMillan LD, et al. (1995) Fatigue-free ferroelectric capacitors with platinum electrodes. *Nature* 374: 627–629. https://doi.org/10.1038/374627a0
11. Park BH, Kang BS, Bu SD, et al. (1999) Lanthanum-substituted bismuth titanate for use in non-volatile memories. *Nature* 401: 682–684. https://doi.org/10.1038/44352
12. Ishiwara H (2012) Ferroelectric random access memories. *J Nanosci Nanotechnol* 12: 7619–7627. https://doi.org/10.1166/jnn.2012.6651
13. Park MH, Lee YH, Mikolajick T, et al. (2018) Review and perspective on ferroelectric HfO_2-based thin films for memory applications. *MRS Commun* 8: 795–808. https://doi.org/10.1557/mrc.2018.175.

14. Jiang H, Gomez-Abal RI, Rinke P, et al. (2010) Electronic band structure of zirconia and hafnia polymorphs from the GW perspective. *Phys Rev B* 81: 85119. https://doi.org/10.1103/PhysRevB.81.085119.
15. Martin D, Yurchuk E, Müller S, et al. (2013) Downscaling ferroelectric field effect transistors by using ferroelectric Si-doped HfO_2. *Solid State Electron* 88: 65–68. https://doi.org/10.1016/j.sse.2013.04.013
16. Müller J, Polakowski P, Mueller S, et al. (2015) Ferroelectric hafnium oxide based materials and devices: Assessment of current status and future prospects. *ECS J Solid State Sci Technol* 4: N30–N35. https://doi.org/10.1149/2.0081505jss.
17. Sang X, Grimley ED, Schenk T, et al. (2015) On the structural origins of ferroelectricity in HfO_2 thin films. *Appl Phys Lett* 106: 162905. https://doi.org/10.1063/1.4919135
18. Shimizu T, Katayama K, Kiguchi T, et al. (2016) The demonstration of significant ferroelectricity in epitaxial Y-doped HfO_2 film. *Sci Rep* 6: 32931. https://doi.org/10.1038/srep32931
19. Park MH, Schenk T, Fancher CM, et al. (2017) A comprehensive study on the structural evolution of HfO_2 thin films doped with various dopants. *J Mater Chem C* 5: 4677–90. https://doi.org/10.1039/C7TC01200D.
20. Shandalov M, Mcintyre P (2009) Size-dependent polymorphism in HfO_2 nanotubes and nanoscale thin films. *J Appl Phys* 106: 84322. https://doi.org/10.1063/1.3243077
21. Muller J, Boscke TS, Schroder U, et al. (2012) Ferroelectricity in simple binary ZrO_2 and HfO_2. *Nano Lett* 12: 4318–23. https://doi.org/10.1021/nl302049k
22. Lomenzo PD, Zhao P, Takmeel Q, et al. (2014) Ferroelectric phenomena in Si-doped HfO_2 thin films with TiN and Ir electrodes. *J Vac Sci Technol B, Nanotechnol Microelectron Mater Process Meas Phenom* 32: 03D123. https://doi.org/10.1116/1.4873323
23. Chernikova AG, Kozodaev MG, Negrov DV, et al. (2018) Improved ferroelectric switching endurance of La-doped $Hf_{0.5}Zr_{0.5}O_2$ thin films. *ACS Appl Mater Interfaces* 10: 2701–8. https://doi.org/10.1021/acsami.7b15110
24. Hoffmann M, Schroeder U, Schenk T, et al. (2015) Stabilizing the ferroelectric phase in doped hafnium oxide. *J Appl Phys* 118: 72006. https://doi.org/10.1063/1.4927805
25. Lee YH, Kim HJ, Moon T, et al. (2017) Preparation and characterization of ferroelectric $Hf_{0.5}Zr_{0.5}O_2$ thin films grown by reactive sputtering. *Nanotechnology* 28: 305703. https://doi.org/10.1088/1361-6528/aa7624
26. Lyu J, Fina I, Bachelet R, et al. (2019) Enhanced ferroelectricity in epitaxial $Hf_{0.5}Zr_{0.5}O_2$ thin films integrated with Si (001) using $SrTiO_3$ templates. Appl Phys Lett 114: 222901. https://doi.org/10.1063/1.5096002
27. Lu YW, Shieh J, Tsai FY (2016) Induction of ferroelectricity in nanoscale ZrO_2/HfO_2 bilayer thin films on $Pt/Ti/SiO_2/Si$ substrates. *Acta Mater* 115: 68–75. https://doi.org/10.1016/j.actamat.2016.05.029
28. Park MH, Kim HJ, Lee G, et al. (2019) A comprehensive study on the mechanism of ferroelectric phase formation in hafnia-zirconia nanolaminates and superlattices. *Appl Phys Rev* 6: 041403. https://doi.org/10.1063/1.5118737.
29. Polakowski P, Müller J (2015) Ferroelectricity in undoped hafnium oxide. *Appl Phys Lett* 106: 232905. https://doi.org/10.1063/1.4922272

30. Cho HW, Pujar P, Choi M, et al. (2021) Direct growth of orthorhombic $Hf_{0.5}Zr_{0.5}O_2$ thin films for hysteresis-free MoS_2 negative capacitance field-effect transistors. *Npj 2D Mater Appl* 5: 46. https://doi.org/10.1038/s41699-021-00229-w.
31. Nukala P, Antoja-Lleonart J, Wei Y, et al. (2019) Direct epitaxial growth of polar (1-X)HfO_2-(x)ZrO_2 ultrathin films on silicon. *ACS Appl Electron Mater* 1: 2585–2593. https://doi.org/10.1021/acsaelm.9b00585.
32. Krebs H-U, Weisheit M, Faupel J, et al. (2003) Pulsed laser deposition (PLD)—A versatile thin film technique, In: Kramer B, *Advances in Solid State Physics*, Springer Berlin, Heidelberg, 505–518. https://doi.org/10.1007/978-3-540-44838-9_36.
33. Enkelmann V (1998) The oligomeric approach, In: Mullen K, Wegner G, 2 Eds., *Electronic Materials*, Wiley: Chichester, 295.
34. Lyu J, Fina I, Solanas R, et al. (2019) Growth window of ferroelectric epitaxial $Hf_{0.5}Zr_{0.5}O_2$ thin films. *ACS Appl Electron Mater* 1: 220–228. https://doi.org/10.1021/acsaelm.8b00065
35. Gunst T, Stradi D, Blom A (2020) Identification of zirconia and hafnia crystalline phases by optical spectroscopy from first-principles, *Nanoengineering: Fabrication, Properties, Optics, Thin Films, and Devices XVII*, 11467: 1146708. https://doi.org/10.1117/12.2568807.
36. Gao L, Yalon E, Chew AR, et al. (2017) Effect of oxygen vacancies and strain on the phonon spectrum of HfO_2 thin films. *J Appl Phys* 121: 224101. https://doi.org/10.1063/1.4984833.
37. Tan T, Liu Z, Lu H, et al. (2010) Structure and optical properties of HfO_2 thin films on silicon after rapid thermal annealing. *Opt Mater (Amst)* 32: 432–435. https://doi.org/10.1016/j.optmat.2009.10.003.
38. Böscke TS, Müller J, Bräuhaus D, et al. (2011) Ferroelectricity in hafnium oxide thin films. Appl Phys Lett 99: 102903. https://doi.org/10.1063/1.3634052
39. Park JH, Kim BK, Park JG, et al. (1999) Dielectric hysteresis measurement in lossy ferroelectrics. *Ferroelectrics* 230: 151–156. https://doi.org/10.1080/00150199908214911.
40. Pandian MS, Ramasamy P, Kumar B (2012) A comparative study of ferroelectric triglycine sulfate (TGS) crystals grown by conventional slow evaporation and unidirectional method. *Mater Res Bull* 47: 1587–1597. https://doi.org/10.1016/j.materresbull.2012.01.030

AIMS Press

© 2023 the Author(s), licensee AIMS Press. This is an open access article distributed under the terms of the Creative Commons Attribution License (http://creativecommons.org/licenses/by/4.0)